Rational Design of NIR-II AIEgens with Ultrahigh Quantum Yields for Photo- and Chemiluminescence Imaging

Hanchen Shen,[1,#] Feiyi Sun,[1,#] Xinyan Zhu,[2,#] Jianyu Zhang,[1] Xinwen Ou,[1] Jianquan Zhang,[1] Changhuo Xu,[1] Herman H. Y. Sung,[1] Ian D. Williams,[1] Sijie Chen,[3] Ryan T. K. Kwok,[1] Jacky W. Y. Lam,[1] Jianwei Sun,[1] Fan Zhang,*[,2] and Ben Zhong Tang*[,1,3,4,5]

[1]Department of Chemistry, Hong Kong Branch of Chinese National Engineering Research Center for Tissue Restoration and Reconstruction, Guangdong-Hong Kong-Macau Joint Laboratory of Optoelectronic and Magnetic Functional Materials, Division of Life Science, and State Key Laboratory of Molecular Neuroscience, The Hong Kong University of Science and Technology, Kowloon, Hong Kong, China. Email: tangbenz@cuhk.edu.cn

[2]Department of Chemistry, State Key Laboratory of Molecular Engineering of Polymers, Shanghai Key Laboratory of Molecular Catalysis and IChEM, Fudan University, Shanghai 200433, P.R. China. Email: zhang_fan@fudan.edu.cn

[3]Ming Wai Lau Centre for Reparative Medicine, Karolinska Institutet, Hong Kong, China.

[4]School of Science and Engineering, Shenzhen Institute of Aggregate Science and Technology, The Chinese University of Hong Kong, Shenzhen, Guangdong 518172, P.R. China.

[5]Guangdong Provincial Key Laboratory of Luminescence from Molecular Aggregates, South China University of Technology, Guangzhou 510640, P.R. China.

[#]H. S., F. S., and X. Z. contributed equally.

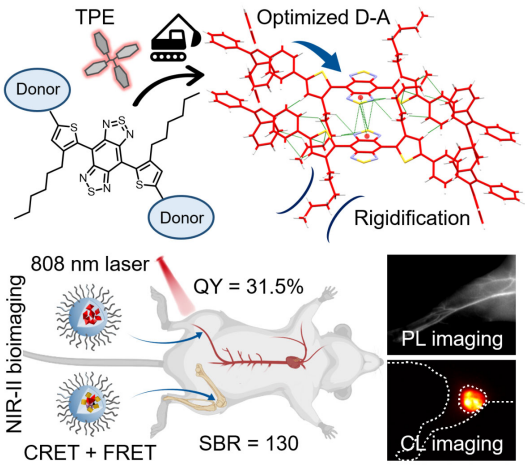

Abstract

Fluorescence imaging in the second near-infrared window (NIR-II, 1000–1700 nm) using small-molecule dyes is highly potential for clinical use. However, many NIR-II dyes suffer from the emission quenching effect and extremely low quantum yields (QYs) in the practical usage forms. The AIE strategy has been successfully utilized to develop NIR-II dyes with donor-acceptor (D-A) structures with acceptable QYs in the aggregate state, but there is still a large room for QY improvement. Here, we rationally designed NIR-II emissive dye named TPE-BBT and its derivative (TPEO-BBT) by changing the electron-donating triphenylamine unit to tetraphenylethlene (TPE). Their nanoparticles exhibited ultrahigh relative QYs of 31.5% and 23.9% in water, respectively. By using an integrating sphere, the absolute QY of TPE-BBT nanoparticles was measured to be 1.8% in water. Its crystals showed an absolute QY of 10.4%, which is the highest value among organic small molecules reported so far. The optimized D-A interaction and the higher rigidity of TPE-BBT in the aggregate state are believed to be the two key factors for its ultrahigh QY. Finally, we utilized TPE-BBT for NIR-II photoluminescence (PL) and chemiluminescence (CL) bioimaging through successive CL resonance energy transfer and Förster resonance energy transfer processes. The ultrahigh QY of TPE-BBT realized an excellent PL imaging quality in mouse blood vessels, and an excellent CL imaging quality in the local arthrosis inflammation in mice with a high signal-to-background ratio of 130. Thus, the design strategy presented here brings new possibilities for the development of bright NIR-II dyes and NIR-II bioimaging technologies.

1. Introduction

Bioimaging is a technology to visualize biological processes in a real-time and non-invasive manner, which plays an important role in the development of medicine by monitoring the physiological processes in the human body. Many imaging modalities have been developed and applied clinically, such as X-ray computed tomography (CT), nuclear magnetic resonance imaging (MRI), and positron emission tomography (PET).[1, 2] However, the present technologies are still suffering from limitations like radioactivity and low sensitivity and resolution. Compared with these traditional imaging modalities, fluorescence imaging is a potential technology for dynamic visualization with advantages of great sensitivity, high resolution, and low cost.[3, 4] Although the fluorescence imaging has now been widely used in many *in vitro* applications, such as immunofluorescence assays and super-resolution imaging,

the poor penetration depth of most fluorescent materials largely impeded their applications *in vivo*. During the past few decades, most fluorescent materials generated photoluminescence (PL) signals in the visible (400–650 nm) and the first near-infrared (NIR-I) region (650–950 nm). On the other hand, the second near-infrared (NIR-II) window (1000–1700 nm) has shown the merits of high signal-to-background ratios (SBRs) and optical resolutions at depths because of reduced interface reflection, autofluorescence, and photon scattering.[5, 6]

Many inorganic NIR-II fluorescent materials have been developed with narrow emission bands and high photostability. However, their applications are still impeded by inevitable drawbacks like low quantum yields (QYs), poor reproducibility, and high toxicity.[7-13] Organic small molecules with NIR-II emission are potential candidates for bioimaging because of good biocompatibility, well-defined molecular structures, and ease of synthetic modification. To red-shift the emission wavelength of NIR-II dyes, two strategies are commonly used.[7, 14] The first strategy is to enlarge the conjugation length. However, it cannot always work practically because of tedious synthesis, unsatisfactory processability, and instability (especially for cyanine dyes with extended double bonds). Another strategy is to design dyes with donor-acceptor (D-A) structures rationally. The D-A strategy can effectively reduce the band gaps through relatively simple synthesis. Unfortunately, the QYs of NIR-II dyes are always extremely low in practical usage. This phenomenon is believed to result from: (1) Most dyes with long-wavelength emission adopt extensively conjugated backbones, and the resultant strong intermolecular interactions may easily cause aggregation-caused quenching (ACQ) effects in concentrated solutions or the aggregate state.[15] (2) The D-A interactions are normally strong, which may cause severe twisted intramolecular charge transfer (TICT) to weaken the emission in polar environments.[16] (3) The band gaps are incredibly narrow, so the formed excitons can easily undergo non-radiative decay pathways by molecular motions.[17] These problems severely retarded the development of NIR-II dyes for bioimaging because the physiological environment is an aqueous medium, where the hydrophobicity of the molecules and the high polarity of the environment can cause an even worse fluorescence quenching effect.

Aggregation-induced emission (AIE) is a unique photophysical phenomenon where AIE-active molecules are non-emissive or weakly emissive in the discrete state because of active intramolecular motions, but show enhanced luminescence upon aggregation due to mechanisms including the restriction of intramolecular motions (RIM), restricted access to a conical intersection, and restriction of access to the dark state.[18-23] Various AIE luminogens (AIEgens) have been developed and have shown great

potential for biomedical applications.[24-26] In NIR-II bioimaging, the AIE strategy is also promising. Many NIR-II AIEgens with acceptable QYs can act as superior imaging materials (the highest QY approaches 15% using IR26 as the reference fluorophore with a QY of 0.5% in 1,2-dichloroethane).[17, 27-29] For instance, our group reported TPA-BBT in 2019, the nanoparticle of which demonstrated a very high QY of about 11% in water.[30] However, the typical D-A-D structure of TPA-BBT caused a strong TICT effect and would suppress its QY in the aqueous solution. Hence, there is still a large room to further raise the QYs of NIR-II AIEgens by optimizing their molecular structures.

Based on the literature review and experimental experience (Scheme 1), we found that the replacement of the triphenylamine (TPA) group with the tetraphenylethlene (TPE) group in D-A-D dyes can largely improve the QYs.[31-34] Until now, few studies have systematically explained this intriguing phenomenon, while we rationally conjecture that this strategy can boost the QYs for NIR-II AIEgens for the following reasons. (1) The TPE group can weaken the D-A interaction to alleviate the TICT effect in the polar environment. (2) TPE has less trend of molecular motion in the aggregate state because the bulkier structure of TPE can bring more intermolecular interactions. (3) There are more covalent bonds attached to the C atom in TPE than the N atom in TPA, also resulting in a stronger RIM effect. The three factors may generate more stabilized excitons when using TPE as the donor group.

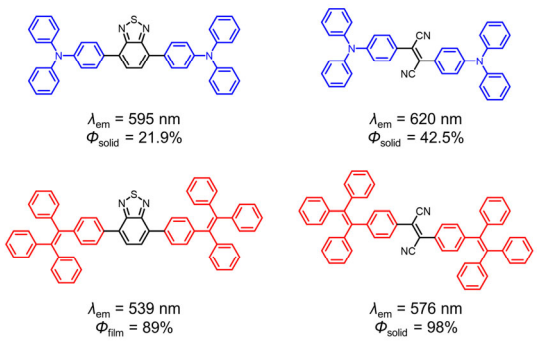

Scheme 1. Photophysical parameters of representative D-A-D dyes with TPA or TPE as the electron donor.

Here, we designed and synthesized two NIR-II emissive AIEgens called TPE-BBT and TPEO-BBT by replacing the TPA group in TPA-BBT with the TPE group (Figure 1a). As expected, the photoluminescent nanoparticles (PLNPs) of TPE-BBT and TPEO-BBT showed much enhanced QYs, which were measured to be 31.5% and 23.9% vs. IR26 (QY = 0.5%), respectively. More importantly, the crystals of TPE-BBT demonstrated an absolute QY of 10.4%, which is the highest absolute QY reported so far. Single-crystal

analysis and theoretical calculations revealed that the optimized D-A interaction and the higher rigidity of TPE-BBT in the aggregate state are the two key factors for its ultrahigh QY. This ultrahigh QY rendered TPE-BBT ideal material for NIR-II photoluminescence (PL) bioimaging. Moreover, TPE-BBT realized NIR-II chemiluminescence (CL) bioimaging, which can avoid the limitation of excitation light sources through successive CL resonance energy transfer (CRET) and Förster resonance energy transfer (FRET) processes.[35] The ultrahigh QY of TPE-BBT ensured a high energy transfer efficiency and excellent continuous imaging for the local arthrosis inflammation detection in mice. Thus, this work revealed a promising strategy to design NIR-II dyes with high QYs and provided insights into the underlying mechanism.

2. Results and discussion

Synthesis and characterization

To investigate the role of different donors, TPA-BBT, TPE-BBT, and TPEO-BBT were synthesized using TPA, TPE, and methoxyl-TPE as electron donors. Their structures were well characterized by ^{1}H NMR, ^{13}C NMR, and high-resolution mass spectra (Figures S1−S6). All three compounds possessed a typical D-A-D structure, where the benzobisthiadiazole (BBT) acted as a strong electron acceptor, and the hexyl unit at the ortho position of thiophene ensured the distorted backbones. We first evaluated the photophysical properties of TPE-BBT and TPEO-BBT. They showed high absorption at 500−800 nm in DMSO, with the molar absorption coefficients larger than 1.4×10^4 M^{-1} cm^{-1} (Figure S7). TPE-BBT PLNPs encapsulated by F127 showed a similar absorption and a strong PL in the region of 900−1200 nm, indicating the potential application of TPE-BBT as a NIR-II imaging agent (Figure 1b). TPE-BBT was weakly emissive in its good solvent DMSO, but was highly emissive in aggregates formed by gradually increasing the fraction of water, suggesting its typical AIE property (Figures 1c and 1d). TPEO-BBT also demonstrated an obvious AIE characteristic in the DMSO/water mixture (Figure S8). The absorption and emission spectra of TPEO-BBT were slightly redshifted relative to those of TPE-BBT, indicating that the electron-donating ability of methoxyl-TPE is stronger than that of TPE. The relative QYs of TPE-BBT, TPEO-BBT, and TPA-BBT in F127 PLNPs were measured using IR26 (QY = 0.5%) as the reference. TPA-BBT PLNPs exhibited a relative QY of 12.7%, which was consistent with out previous result (11%).[30] TPE-BBT and TPEO-BBT PLNPs showed ultrahigh relative QYs of 31.5% and 23.9%, respectively, which are among the highest reported QYs in the aqueous solution (Figure 1e). The

relatively lower QY of TPEO-BBT PLNPs resulted from the stronger D-A interaction, demonstrating the importance of the optimization of the D-A interaction.

The measurement of relative QYs strongly depends on the absolute QYs of reference fluorophores. However, the presented references for NIR-II dyes, such as IR26 and SWCNT, exhibited low QYs. Therefore, the documented QY values of the references would have large deviations, and there is a discrepancy among the documented QY values for the same reference.[36] Thus, the measurement of relative QYs for NIR-II dyes is not accurate. Based on the ultrahigh QY of TPE-BBT, we precisely measured its absolute QY in different states using an integrating sphere (Table 1). Compared to the undetectable absolute QY of TPA-BBT PLNPs, the absolute QY of TPE-BBT PLNPs was detected to be 1.8%, which was an extremely high value for NIR-II dyes. According to the changes in PL intensity in different water fractions (f_w), TPE-BBT demonstrated a sharp increase in PL intensity at the f_w = 20%, and the PL intensity gradually decreased afterwards. The size distributions and morphologies of TPE-BBT nanoaggregates at f_w = 20%, 50%, and 99% were characterized by dynamic light scattering (DLS) and scanning electron microscope (SEM), respectively (Figures 1f and 1g). TPE-BBT began to form large aggregates with a mean diameter (d) of 629 nm at f_w = 20%, and the size of formed aggregates decreased when the f_w increased to 50% (d = 203 nm) or 90% (d = 82 nm). The absolute QYs of three aggregates in different f_w were measured. The largest aggregates at f_w = 20% showed the highest QY of 4.6%, while smaller aggregates displayed reduced QY values of 3.4% at f_w = 50% and 2.1% at f_w = 99% (Figure 1g). This phenomenon suggested that the QY of TPE-BBT was related to the size of aggregates. It is understandable because when the size of aggregates decreases, there will be more free molecules on the surface of the aggregates. They will undergo active molecular motions because of the lack of spacial restriction, resulting in an enhanced non-radiative decay and a relatively lower QY.[37] Similarly, both powders and crystals of TPE-BBT demonstrated higher absolute QYs than its PLNPs and aggregates because of the higher degree of aggregation (Table 1).

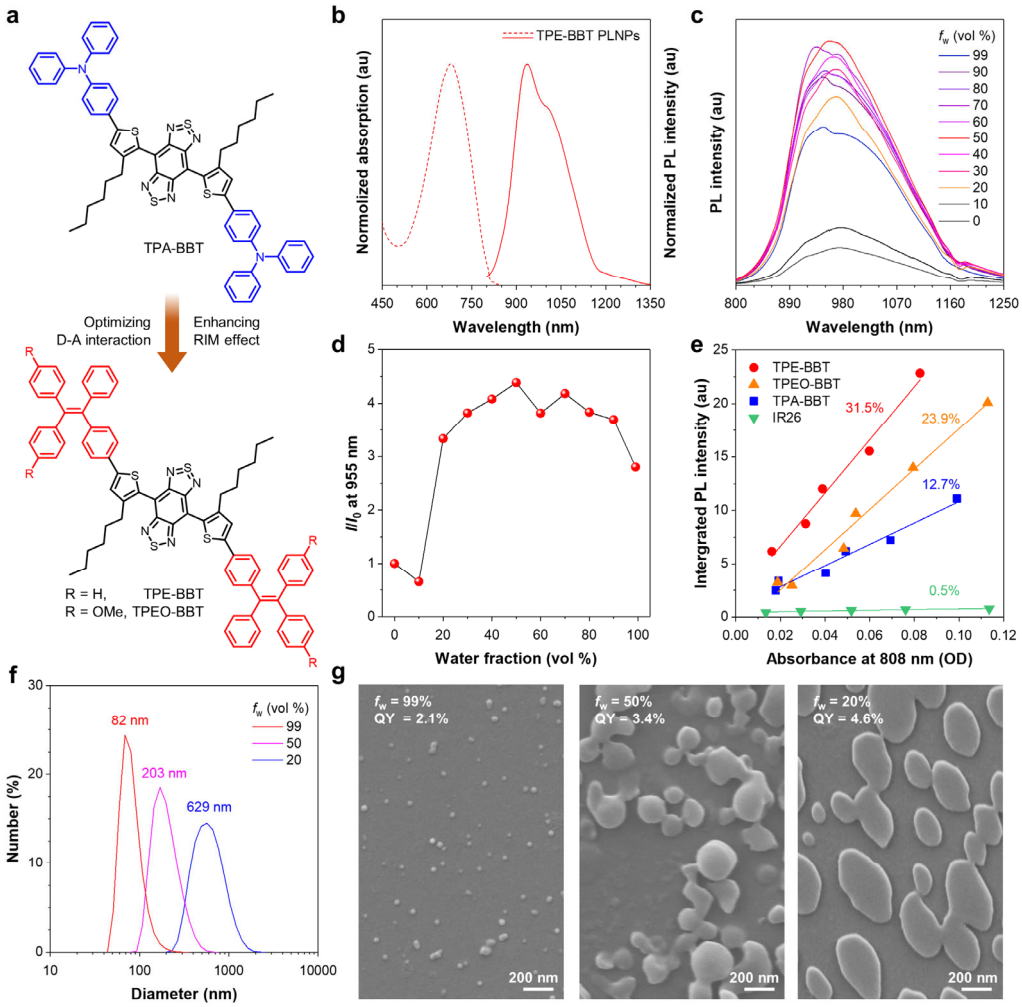

Figure 1. (a) Chemical structures of TPA-BBT, TPE-BBT, and TPEO-BBT. (b) Normalized absorption (dashed line) and PL (solid line) spectra of TPE-BBT photoluminescent nanoparticles (PLNPs) encapsulated by F127 in water. (c) Photoluminescence (PL) spectra of TPE-BBT in DMSO/water mixtures at different water fractions (f_w). Molecular concentration: 10^{-5} M; λ_{ex} = 660 nm. (d) Plots of relative PL intensity of TPE-BBT at 955 nm (I/I_0) versus f_w. Molecular concentration: 10^{-5} M; λ_{ex} = 660 nm; I_0 = emission intensity in DMSO (f_w = 0%). (e) Plots of the integrated PL spectra of TPA-BBT, TPE-BBT, TPEO-BBT PLNPs (850–1600 nm in water) and IR26 (850–1600 nm in 1,2-dichloroethane, QY = 0.5%) at five different concentrations. (f) Size distributions of TPE-BBT aggregates in DMSO/water mixtures with f_w of 99%, 50%, and 20%. (g) SEM images of TPE-BBT aggregates in DMSO/water mixtures with f_w of 99%, 50%, and 20%, respectively. Absolute QYs (850–1600 nm) of TPE-BBT in different states were measured by an integrating sphere. λ_{ex} = 808 nm.

Table 1. Absolute QYs of TPE-BBT and TPA-BBT[a]

AIEgen	QY_{PLNP} (%)[b]	$QY_{Aggregate}$ (%)[c]	QY_{Powder} (%)[d]	$QY_{Crystal}$ (%)
TPE-BBT	1.8	2.1	4.9	10.4
TPA-BBT	<1	<1	1.8	3.3

[a]Absolute QYs measured by an integrating sphere. λ_{ex} = 808 nm. [b]TPE-BBT and TPA-BBT PLNPs (d < 30 nm). [c]Aggregates of TPE-BBT formed in the DMSO/water mixture (f_w = 99%) and aggregates of TPA-BBT formed in THF/water mixture (f_w = 99%). [d]Powders generated via a precipitation process in methanol.

The QYs of TPE-BBT in all states are higher than those of TPA-BBT (Table 1). To gain deeper insights into the photophysical properties of TPE-BBT and TPA-BBT, their single-crystal structures were obtained and analyzed. Both TPE-BBT and TPA-BBT had a layer-by-layer packing mode (Figures 2a and 2d). The BBT cores of both molecules were immobilized by S···S, N···N, and S···π interactions, while there were more intermolecular interactions between two closely contacted TPE-BBT within one layer (d_1–d_{14}) than those in TPA-BBT (d_1–d_6) (Figures 2b and 2e). In TPE-BBT crystals, the molecular motions of alkyl chains were strongly restricted by C-H···S, C-H···N, and C-H···π interactions (d_4–d_{10} and d_{12}–d_{14}). In comparison, the flexible alkyl chains in TPA-BBT were less affected by these interactions, which provided a liquid-like environment for active molecular motions. In addition, the comparison of their intermolecular interactions between two closely contacted molecules in two nearby layers revealed that both molecules had 5 short-range interactions and thus had a similar degree of restriction of molecular motions (Figures 2c and 2f). Considering the intermolecular interactions of two closely contacted molecules in different directions, it is clear that TPE-BBT boasted stronger intermolecular interactions, while TPA-BBT would undergo more vigorous molecular motions upon photoexcitation. Thus, TPA-BBT showed a lower QY than TPE-BBT in the crystalline state.

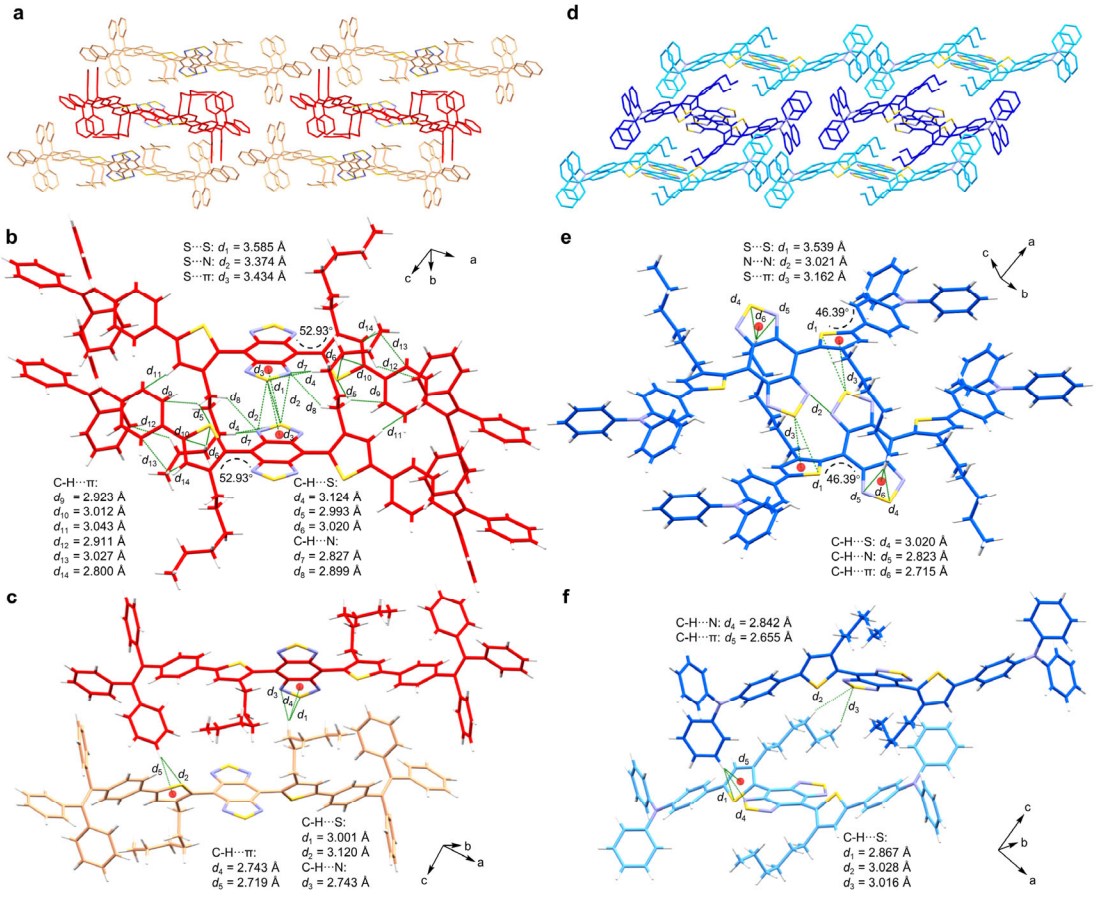

Figure 2. Single-crystal analysis of TPE-BBT and TPA-BBT. (a) Molecular packing and (b and c) intermolecular interactions of two closely contacted TPE-BBT in different directions. (d) Molecular packing and (e and f) intermolecular interactions of two closely contacted TPA-BBT in different directions.

Theoretical calculation

Molecular dynamics (MD) simulations were first conducted to better understand the molecular stacking mode in the aggregate state. 20 molecules of TPE-BBT and TPA-BBT were placed in a cubic box with a length of 10 nm and relaxed to obtain the amorphous aggregate conformation. The aggregates were then solvated by water molecules to study their behaviors in water (Figures 3a and Figure S9). The properties of single molecules in different environments were also investigated, and the details of these simulations are shown in the supporting information. To investigate the molecular motions of TPE-BBT and TPA-BBT under different conditions, we calculated the dihedral angle between the thiophene and BBT core of the innermost molecule, which represented a major rotor. Dihedral angles of the innermost molecules in TPE-BBT and TPA-BBT aggregates showed a wide distribution in the single-molecule state, which

suggested their free rotations (Figure S10). However, the distributions became narrow when they formed under vacuum, indicating the effect of RIM. Interestingly, when the aggregates were solvated by water, the distribution of the dihedral angles for TPE-BBT was further narrowed, while that of TPA-BBT became broader (Figure 3c). To explain the change of dihedral angles, the inner part of TPE-BBT and TPA-BBT aggregates were studied (Figure S11). Water molecules could hardly be found inside TPE-BBT aggregates. However, water molecules appeared close to the core part of the innermost TPA-BBT. The penetration of water molecules not only loosened the aggregates to reduce the RIM effect, but also provided a more polar environment for TPA-BBT, which should cause a severe TICT effect to reduce the fluorescence intensity. The atomic contact ratios of the innermost TPE-BBT and TPA-BBT were also calculated (Figure 3d). TPE-BBT showed a higher contact ratio, which meant that a higher ratio of atoms in TPE-BBT interacted with surrounding organic molecules and the atomic fluctuations could be restricted. This result indicated a higher degree of RIM for TPE-BBT aggregates in water. Finally, to quantitatively evaluate the intermolecular interactions, the interaction energy (composed of electrostatic energy and van der Waals energy) of the innermost molecule with surrounding organic molecules was calculated (Figures 3e and S12). The innermost TPE-BBT had much higher interaction energy than TPA-BBT, further proving the higher extent of RIM for TPE-BBT aggregates in water.

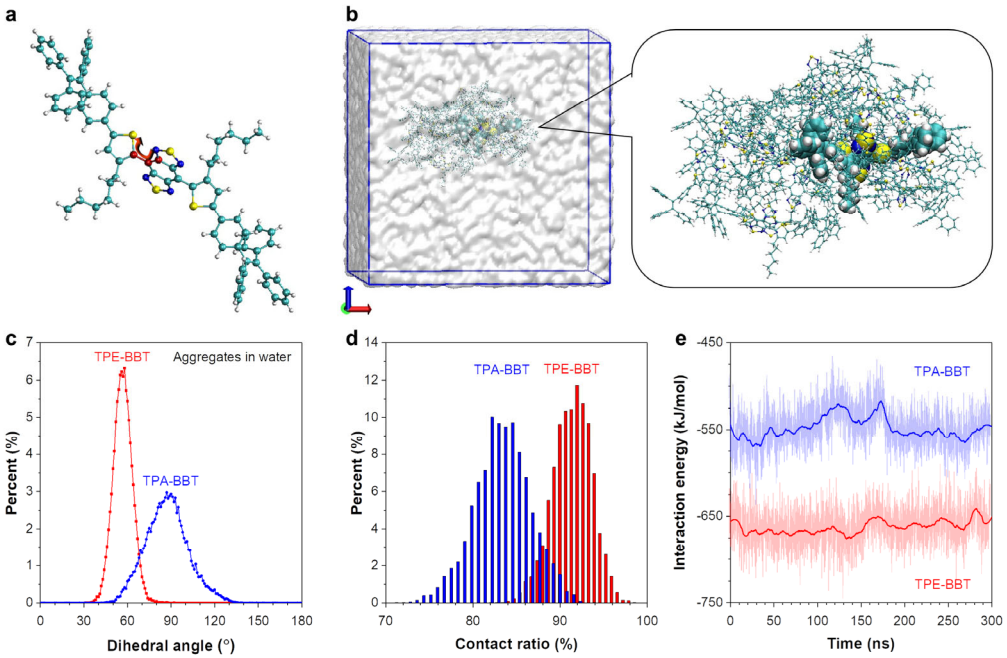

Figure 3. (a) Molecular conformation of TPE-BBT. The red arrow indicates the dominant dihedral angle between the thiophene and the BBT core. (b) Molecular dynamics simulation snapshot of TPE-BBT aggregates in water. The innermost molecule was shown in spacefill style, while the other molecules were shown in ball and stick style. (c) The distributions of the representative dihedral angle (between the thiophene and the BBT core) of the innermost molecules in TPE-BBT and TPA-BBT aggregates in water. (d) The atomic contact ratio distributions of the innermost molecules in TPE-BBT and TPA-BBT aggregates in water. (e) The total interaction energy (composed of electrostatic energy and van der Waals energy) of the innermost molecules in TPE-BBT and TPA-BBT aggregates at different times.

Furthermore, density functional theory (DFT) calculations were conducted to show its electronic properties. The ground-state geometries of TPE-BBT and TPA-BBT were optimized first (Figure S13). The highest occupied molecular orbitals (HOMO) of both molecules were delocalized along the conjugated backbone, while the lowest unoccupied molecular orbitals (LUMO) were located mainly on the BBT core (Figures 4a and 4d). The energy gap between HOMO and LUMO in TPE-BBT was slightly larger than that of TPA-BBT, because the electron-donating ability of TPE moiety is weaker than that of TPA moiety. The weaker D-A interaction in TPE-BBT can intrinsically reduce the dark TICT effect and ensure a high QY. Besides, we also quantitatively analyzed the intramolecular motions of TPE-BBT (Figures 4b and 4c) and TPA-BBT (Figures 4e and 4f) in both the gas phase and crystalline phase by reorganization energy calculation. Normal modes in the low-frequency region are contributed by the

changes of dihedral angels and are closely related to non-radiative decay.[30] For both molecules, the contribution from dihedral angles largely decreased in the crystalline, compared with that in the gas phase. However, the decrement of TPE-BBT (from 32.94% to 10.94%) was obviously larger than that of TPA-BBT (from 20.87% to 12.36%). Thus, the above results also proved that TPE-BBT possessed a stronger RIM effect than TPA-BBT, contributing to its higher QYs in aggregate and solid states.

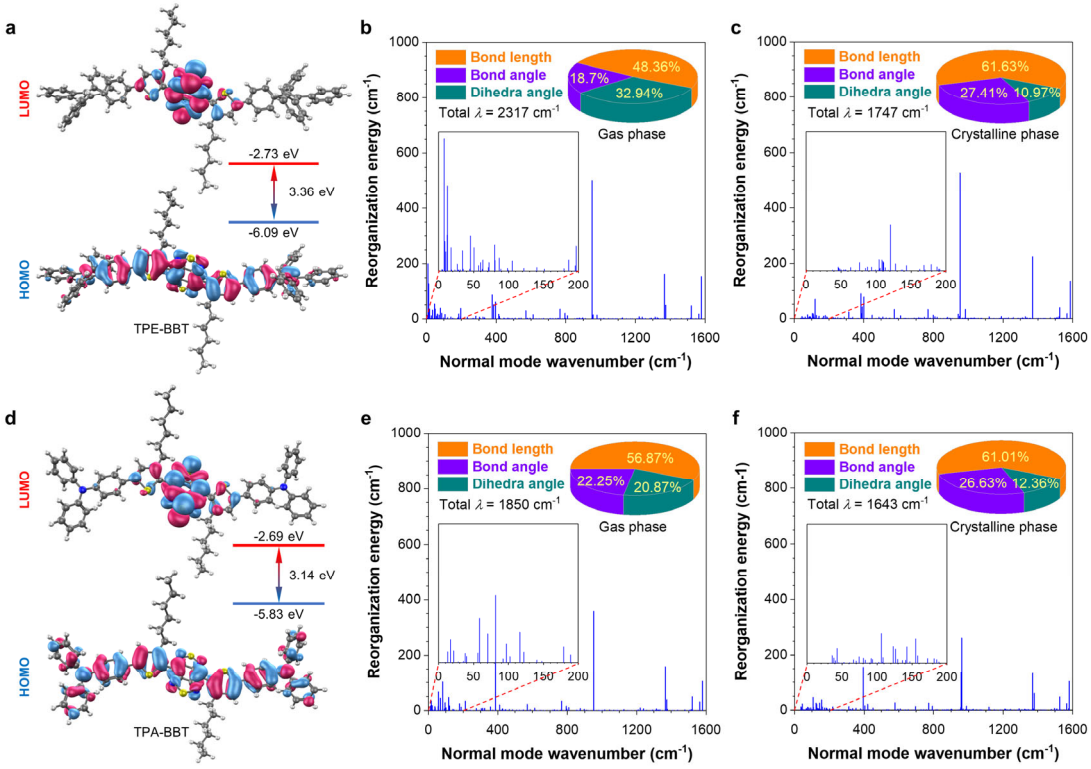

Figure 4. (a, d) Frontier molecular orbitals of (a) TPE-BBT and (d) TPA-BBT based on the optimized ground-state geometries. (b, c) Plots of reorganization energy vs. normal mode wavenumber of TPE-BBT in the (b) gas and (c) crystalline phases. Inset: proportions of bond length, bond angle, and dihedral angle contributed to total reorganization energy (λ). (e, f) Plots of reorganization energy vs. normal mode wavenumber of TPA-BBT in the (e) gas and (f) crystalline phases.

NIR-II PL performance of PLNPs for blood vessel imaging

The NIR-I absorption and NIR-II emission made TPE-BBT a potential candidate for NIR-II bioimaging *in vivo*. Here we evaluate the performance of TPE-BBT PLNPs for NIR-II vascular imaging. The DLS spectrum and TEM image proved that TPE-BBT PLNPs had a homogeneous spherical structure (d < 30 nm) (Figure 5a). Besides, the cytotoxicity assay using human umbilical vein endothelial cells (HUVEC) demonstrated that TPE-BBT had negligible toxicity even when the molecular concentration reached 1 mg/ml (Figure 5b). In addition, both TPE-BBT and TPEO-BBT PLNPs showed superior photostability

to the commercial NIR contrast agent indocyanine green (ICG) (Figure 5c). These results confirmed the potential of TPE-BBT in biological applications. TPA-BBT PLNPs were also prepared, and the NIR-II imaging qualities in mouse models were compared using TPE-BBT PLNPs, TPA-BBT PLNPs, and ICG, respectively. The PLNPs and ICG were intravenously injected (100 μL, molecular concentration = 1 mg/mL), and an InGaAs camera recorded the angiographies with 850 and 1000 nm long-pass (LP) filters (Figure 5d–f). All three dyes showed good imaging clarity of blood vessels in the hindlimbs, while TPA-BBT PLNPs showed better imaging resolution than ICG, which was consistent with our previous conclusions.[30] TPE-BBT PLNPs demonstrated the best imaging quality, with the smallest full width at half maximums (FWHM) of 0.23 mm and the highest SBR of 1.76 (Figure 5g–h). This result implied that higher brightness in the NIR-II window is essential for better imaging quality.

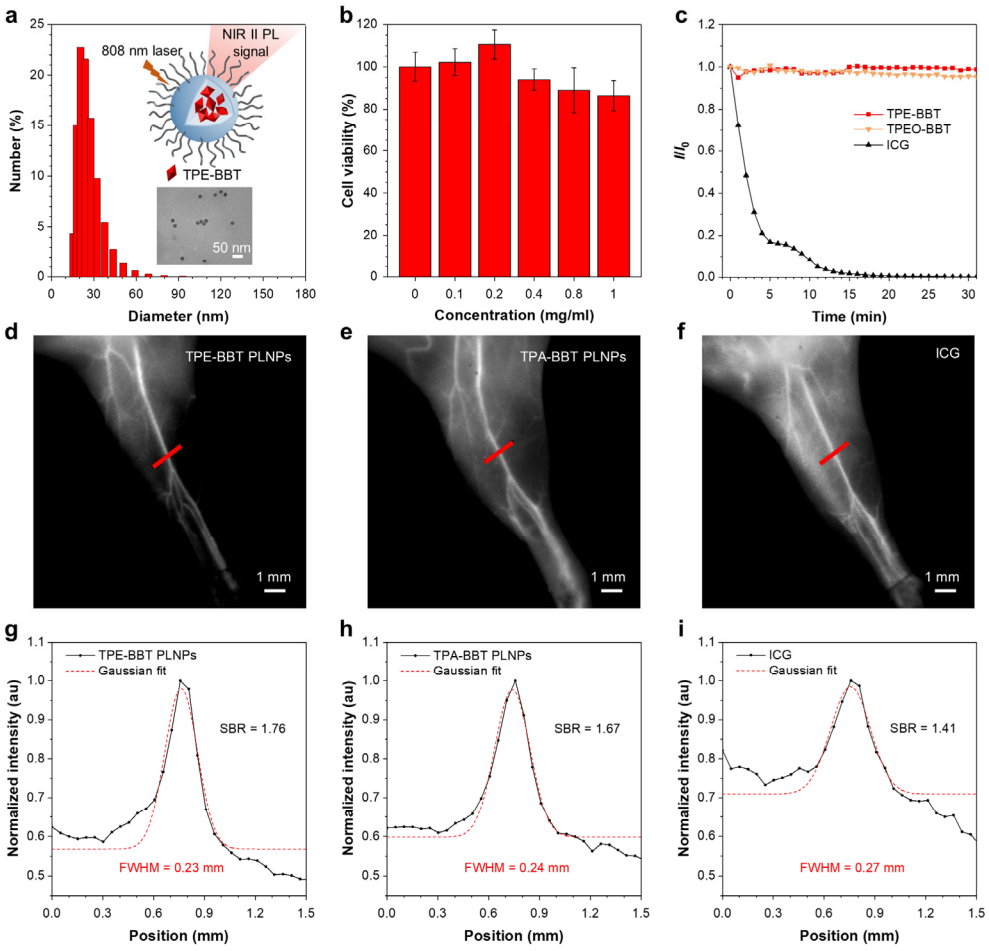

Figure 5. (a) Size distribution (d = 25 nm) of TPE-BBT PLNPs. Insets: schematic diagram and TEM image of TPE-BBT PLNPs. (b) Cell viability of human umbilical vein endothelial cells (HUVECs) treated by different concentrations of TPE-BBT PLNPs for 24 h. Data represent means ± standard deviation (SD). (c) Plots of relative photoluminescence intensity (I/I_0) at corresponding emission peaks (TPE-BBT: 950 nm; TPEO-BBT: 950 nm; ICG: 900nm) under continuous irradiation (0.9 W/cm^2), where I_0 and I

were the fluorescence peak intensity before and after laser irradiation, respectively. (d–f) NIR-II fluorescence imaging of blood vessels in hindlimb post the intravenous injection of 100 μL (d) TPE-BBT PLNPs, (e) TPA-BBT PLNPs, and (f) ICG, respectively. Molecular concentration: 1 mg/mL; λ_{ex} = 808 nm; power density = 30 mW cm^2; 850 and 1000 nm LP filter; exposure time = 100 ms. (g–i) Cross-sectional fluorescence intensity profiles along the red lines in blood vessels treated by (g) TPE-BBT PLNPs, (h) TPA-BBT PLNPs, and (i) ICG, respectively. Gaussian fits are shown in red dashed lines.

NIR-II CL performance of CLNPs for arthrosis inflammation imaging

CL imaging, especially NIR-II CL imaging, can conquer the limitation of excitation light to ensure deep tissue penetration, high SBR, and high sensitivity.[35, 38-42] However, there is still big space for improving the QY of the CL imaging systems. This problem could be solved by utilizing NIR-II dyes with high QYs as energy acceptors. Here we designed an efficient NIR-II CL imaging system, which was realized by successive CL resonance energy transfer (CRET) and Förster resonance energy transfer (FRET) processes (Figure 6a). The TPE-BBT chemiluminescent nanoparticles (CLNPs) were dispersed by F127 in water, co-encapsulated with bis[3,4,6-trichloro-2-(pentyloxycarbonyl)phenyl]oxalate (CPPO) and a D-A-D fluorescent dyes named BTD540. CPPO was chosen as the peroxyoxalate. Theoretically, CPPO would first react with H_2O_2 to generate 1,2-dioxetanedione intermediate (DOD), and then BTD540 would be excited by the high-energy DOD. Successively, NIR-II photons could be generated through a FRET process between NIR-I emissive BTD540 and NIR-II emissive TPE-BBT. The DLS data and TEM image showed that TPE-BBT CLNPs were successfully prepared with an average diameter of 30 nm (Figure 6b). BTD540 and TPE-BBT in nanoparticles showed large Stokes shifts, and the emission of BTD540 presented perfect spectral overlap with the absorption of TPE-BBT (Figure 6c). These results ensured an efficient FRET process between BTD540 and TPE-BBT. To verify the FRET process, we measured the PL spectrum of the mixture of BTD540 and TPE-BBT in nanoparticles in water (Figure 6d). The nanoparticles showed no PL signals at 600–800 nm, while the nanoparticles containing only BTD540 showed strong PL signals at the same wavelength range. The disappeared PL signals of BTD540 in the mixture proved the efficient FRET process between BTD540 and TPE-BBT. The prepared TPE-BBT CLNPs could generate a strong NIR-II CL signal upon the addition of H_2O_2. The CL spectrum of TPE-BBT CLNPs matched well with the PL spectrum of TPE-BBT, suggesting the successful energy transfer process in this CL imaging system (Figure 6e). To study the importance of the QY of NIR-II AIEgens in building an efficient NIR-II CL imaging system, TPA-BBT CLNPs were also prepared through a similar

method to TPE-BBT CLNPs, except that TPA-BBT was used as the NIR-II energy acceptor. The spectral studies also indicated an efficient FRET process between BTD540 and TPA-BBT (Figure S14). Then, the response to H_2O_2 of these two prepared CLNPs were tested, respectively. Both CLNPs were effectively lightened at room temperature upon the addition of H_2O_2, and the CL intensity increased at higher concentrations of H_2O_2 (Figure S15). The CL intensities and CL persistency of TPE-BBT and TPA-BBT CLNPs in 2.73% H_2O_2 aqueous solutions were compared (Figures 6f and 6g). The CL signals of both CLNPs were strongest at 50−100 min after the addition of H_2O_2. The CL signal from TPE-BBT CLNPs was about three times stronger than that of TPA-BBT CLNPs at 90 min, which is consistent with the difference between two NIR-II AIEgens in QY. These results suggested the importance of NIR-II energy acceptors with high QYs in the CL imaging systems, and proved that TPE-BBT CLNPs were a potential candidate for CL imaging.

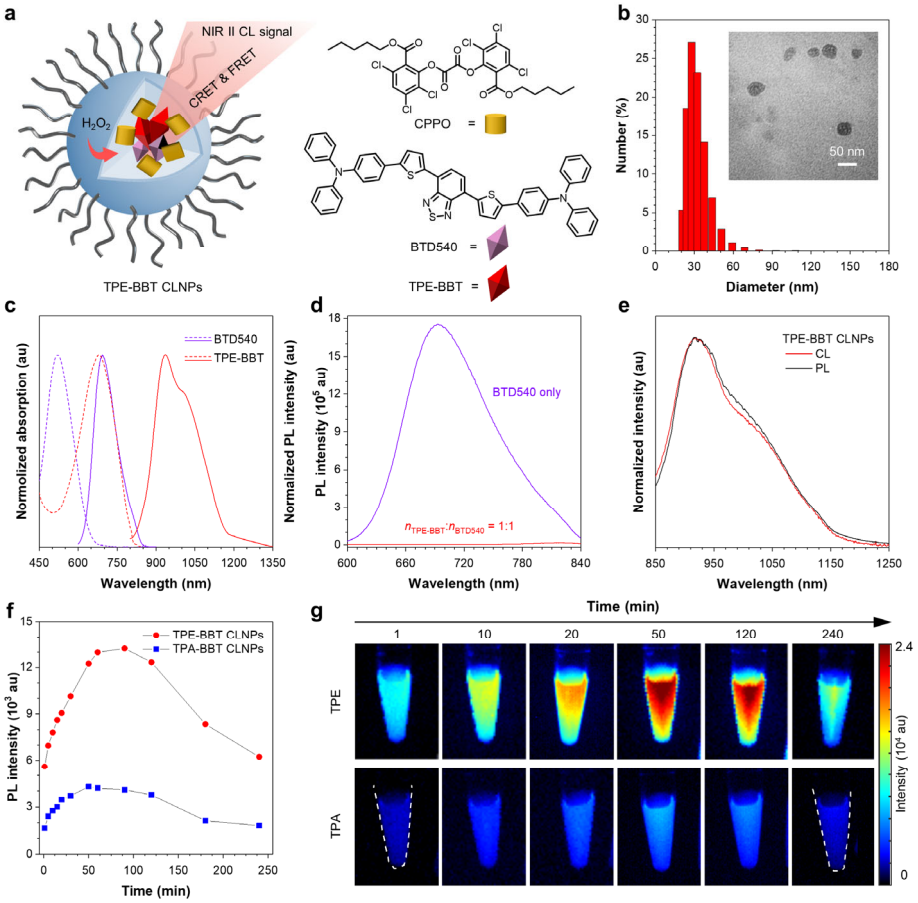

Figure 6. (a) Schematic illustration of the fabrication of TPE-BBT chemiluminescent nanoparticles (CLNPs) using F127 as the surfactant. (b) DLS spectrum (d = 32 nm) and TEM image of TPE-BBT CLNPs. (c) Normalized absorption (dashed line) and emission (solid line) spectra of BTD540 (purple line) and TPE-BBT (red line) in nanoparticles in water. (d) Photoluminescence (PL) spectra of BTD540 and BTD540/TPE-BBT (molar ratio = 1:1) in nanoparticles in water. (e) PL and chemiluminescence (CL)

spectra of TPE-BBT CLNPs in a 2.73% H_2O_2 aqueous solution. λ_{ex} = 808 nm. (f) Time-dependent CL intensity of TPE-BBT and TPA-BBT CLNPs in 2.73% H_2O_2 aqueous solutions. (g) Time-dependent CL imaging of TPE-BBT CLNPs and TPA-BBT CLNPs in 2.73% H_2O_2 aqueous solutions.

The excellent CL imaging ability of TPE-BBT CLNPs *in vitro* encouraged us further to explore its application for NIR-II CL imaging *in vivo*. As shown in Figure 7a, the arthrosis inflammation model of mice was established by intra-articular injection of 70 μL of H_2O_2 solution (100 mM). Then, 0.66 mg of TPE-BBT or TPA-BBT CLNPs were injected into the arthrosis of mice. After the injection of two CLNPs for 2 min, strong CL signals appeared in both inflammation areas (Figure 7b). The intensity profiles along the arthrosis position (Line 1 and Line 2 in Figure 7b) showed that TPE-BBT CLNPs had a stronger CL intensity (Figure 7d), and provided more specific imaging for arthrosis inflammation. We then set the arthrosis inflammation as the region of interest (ROI) and recorded the CL signals for a longer time (Figures 7b and 7c). The SBRs in the ROI at different time points were also calculated and recorded in Figure 7e. The CL imaging using TPE-BBT CLNPs demonstrated an extremely high SBR of about 130 at the beginning. Strikingly, the SBR of the CL signal still remained larger than 10 even at 62 min post-injection. The high SBR ensured an excellent imaging quality for long-term tracking. On the other hand, TPA-BBT CLNPs also showed good CL imaging quality, with an SBR of about 10 at 42 min post-injection. However, TPE-BBT CLNPs emitted much stronger CL signals in the whole CL imaging process, and the SBRs were also much larger. These results proved that NIR-II dyes with high QYs played a vital role in NIR-II CLNPs, and TPE-BBT had great potential for clinical CL imaging.

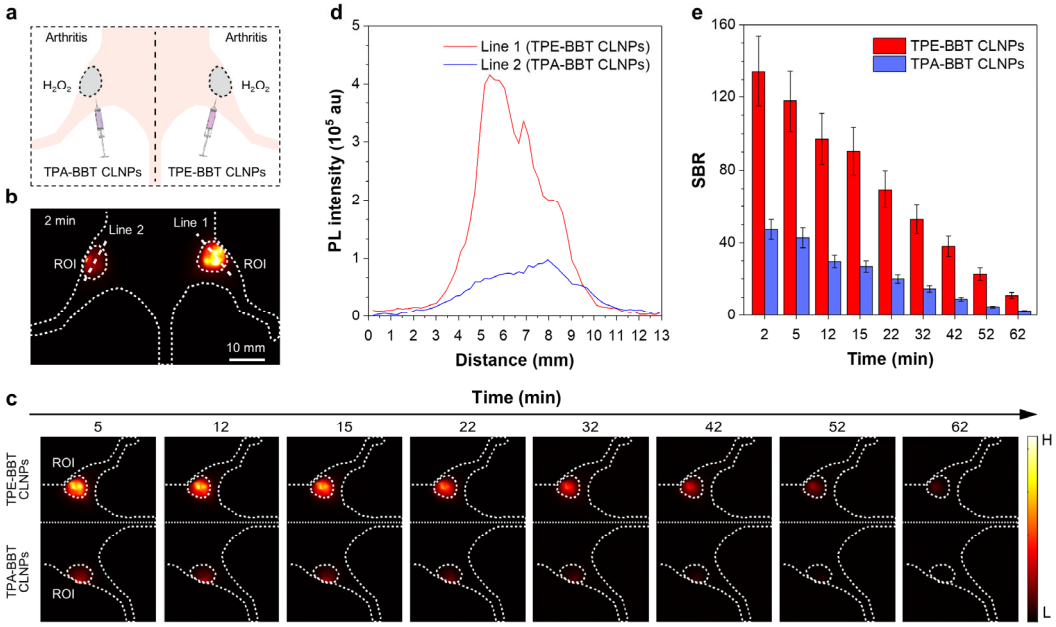

Figure 7. (a) Schematic illustration of chemiluminescence (CL) imaging of the arthrosis in mice. (b) *In vivo* NIR-II CL imaging using 0.66 mg of TPE-BBT (Line 1) and TPA-BBT (Line 2) CLNPs after injection for 2 min. (c) *In vivo* NIR-II CL imaging of arthrosis inflammation using TPE-BBT and TPA-BBT CLNPs at different post-injection times. Exposure time: 10 s. (d) Cross-sectional CL intensity profiles along Line 1 and Line 2 in (b) after injection for 2 minutes. (e) Signal-to-background ratios (SBRs) of the CL intensity in the ROI as a function of post-injection time after the injection of TPE-BBT and TPA-BBT CLNPs. Data represent means ± SD.

3. Conclusions

In summary, we designed and synthesized NIR-II AIEgens with ultrahigh QYs based on the donor engineering. By thorough experimental and theoretical calculations, we revealed the two key factors for obtaining dye molecules with ultrahigh QYs by constructing D-A structures using TPE as a donor. The optimized D-A interaction could mediate the strong TICT effect as the TICT effect would severely quench the luminescence in the aqueous environment. Thus, the mitigation of TICT effect would effectively raise the QY. Because TPA-BBT and TPEO-BBT showed stronger D-A interaction than TPE-BBT, TPE-BBT thus demonstrated the highest QYs in all the states. On the ohther hand, the results of single-crystal analysis, MD simulations, and reorganization energy calculations proved that TPE-BBT demonstrated a stronger RIM effect in aggregates because of the stronger intermolecular interactions.

The enhanced RIM effect of TPE-BBT was beneficial in stabilizing the exciton to result in its ultrahigh QY.

The NIR-I absorption and NIR-II luminescence of TPE-BBT were ideal for the NIR-II photo- and chemiluminescence imaging. TPE-BBT PLNPs were fabricated for blood vessel imaging in the mice model. The results showed that TPE-BBT showed a better SBR and imaging quality than those of TPA-BBT and commercially available ICG, indicating the high potential of TPE-BBT as a PL imaging agent. In the arthrosis inflammation imaging experiments using NIR-II CLNPs, TPE-BBT successfully generated strong NIR-II CL signals. The highest SBR of TPE-BBT CLNPs in the inflammation area was about 130, and the SBRs remained larger than 10 even after 62 min. The CL imaging quality using TPE-BBT CLNPs outperformed that using TPA-BBT, which demonstrated the importance of the QYs of NIR-II energy acceptors. These results also demonstrated that TPE-BBT showed great potential for CL imaging and sensing.

In this work, the mechanism to achieve an ultrahigh QY revealed a possible strategy to develop more bright NIR-II dyes. Also, the ultrahigh QY of TPE-BBT could accelerate the development of excitation-free imaging technologies, including chemi- and bioluminescence imaging and afterglow luminescent imaging.

Acknowledgments

This work was partially supported by the National Natural Science Foundation of China Grant (51773076, 21871060, 81271476, and 31870991), the Innovation and Technology Commission (ITC-CNERC14SC01 and ITCPD/17-9), the Research Grants Council of Hong Kong (16306620, 16303221, C6014-20W and N_HKUST609/19), Ming Wai Lau Centre for Reparative Medicine, Karolinska Institutet (MWLC19SC02), and the Material Science Foundation of Guangdong Province (2019B121205012 and 2019B030301003).

Reference

1. Lee, S.; Chen, X., Dual-Modality Probes for in Vivo Molecular Imaging. *Mol. Imaging* **2009,** *8*, 87–100.

2. Lei, Z.; Zhang, F., Molecular Engineering of NIR-II Fluorophores for Improved Biomedical Detection. *Angew. Chem. Int. Ed.* **2021,** *60*, 16294–16308.

3. Zhang, J.; Zou, H.; Gan, S.; He, B.; Huang, J. C.; Peng, C.; Lam, J. W. Y.; Zheng, L.; Tang, B. Z., Endowing AIE with Extraordinary Potential: A New Au(I)-Containing AIEgen for Bimodal Bioimaging-Guided Multimodal Synergistic Cancer Therapy. *Adv. Funct. Mater.* **2021,** *32*, 2108199.

4. Xu, C.; Peng, C.; Yang, X.; Zhang, R.; Zhao, Z.; Yan, B.; Zhang, J.; Gong, J.; He, X.; Kwok, R. T. K.; Lam, J. W. Y.; Tang, B. Z., One-Pot Synthesis of Customized Metal-Phenolic-Network-Coated AIE Dots for In Vivo Bioimaging. *Adv Sci (Weinh)* **2022,** *9*, 2104997.

5. Hong, G. S.; Antaris, A. L.; Dai, H. J., Near-infrared fluorophores for biomedical imaging. *Nat. Biomed. Eng.* **2017,** *1*, 0010.

6. Zhao, M.; Li, B.; Zhang, H.; Zhang, F., Activatable fluorescence sensors for in vivo bio-detection in the second near-infrared window. *Chem. Sci.* **2020,** *12*, 3448–3459.

7. Dahal, D.; Ray, P.; Pan, D., Unlocking the power of optical imaging in the second biological window: Structuring near-infrared II materials from organic molecules to nanoparticles. *WIREs Nanomed. Nanobiotechnol.* **2021,** *13*, e1734.

8. Welsher, K.; Liu, Z.; Sherlock, S. P.; Robinson, J. T.; Chen, Z.; Daranciang, D.; Dai, H., A route to brightly fluorescent carbon nanotubes for near-infrared imaging in mice. *Nat. Nanotechnol.* **2009,** *4*, 773–780.

9. Hansen, S. F.; Lennquist, A., Carbon nanotubes added to the SIN List as a nanomaterial of Very High Concern. *Nat. Nanotechnol.* **2020,** *15*, 3–4.

10. Li, Y.; Bai, G.; Zeng, S.; Hao, J., Theranostic Carbon Dots with Innovative NIR-II Emission for in Vivo Renal-Excreted Optical Imaging and Photothermal Therapy. *ACS Appl. Mater. Interfaces* **2019,** *11*, 4737–4744.

11. Pandey, S.; Bodas, D., High-quality quantum dots for multiplexed bioimaging: A critical review. *Adv. Colloid. Interface Sci.* **2020,** *278*, 102137.

12. Sinha, N.; Jiménez, J.-R.; Pfund, B.; Prescimone, A.; Piguet, C.; Wenger, O. S., A Near-Infrared-II Emissive Chromium(III) Complex. *Angew. Chem. Int. Ed.* **2021,** *60*, 23722–23728.

13. Wang, T.; Wang, S.; Liu, Z.; He, Z.; Yu, P.; Zhao, M.; Zhang, H.; Lu, L.; Wang, Z.; Wang, Z.; Zhang, W.; Fan, Y.; Sun, C.; Zhao, D.; Liu, W.; Bünzli, J.-C. G.; Zhang, F., A hybrid erbium(III)-bacteriochlorin near-infrared probe for multiplexed biomedical imaging. *Nat. Mat.* **2021,** *20*, 1571–1578.

14. Wang, S.; Fan, Y.; Li, D.; Sun, C.; Lei, Z.; Lu, L.; Wang, T.; Zhang, F., Anti-quenching NIR-II molecular fluorophores for in vivo high-contrast imaging and pH sensing. *Nat Commun* **2019,** *10*, 1058.

15. Gao, H.; Zhang, X.; Chen, C.; Li, K.; Ding, D., Unity Makes Strength: How Aggregation-Induced Emission Luminogens Advance the Biomedical Field. *Adv. Biosys.* **2018,** *2*, 1800074.

16. Gao, S.; Wei, G.; Zhang, S.; Zheng, B.; Xu, J.; Chen, G.; Li, M.; Song, S.; Fu, W.; Xiao, Z.; Lu, W., Albumin tailoring fluorescence and photothermal conversion effect of near-infrared-II fluorophore with aggregation-induced emission characteristics. *Nat. Commun.* **2019,** *10*, 2206.

17. Liu, S.; Li, Y.; Kwok, R. T. K.; Lam, J. W. Y.; Tang, B. Z., Structural and process controls of AIEgens for NIR-II theranostics. *Chem. Sci.* **2020,** *12*, 3427–3436.

18. Zhao, Z.; Zhang, H.; Lam, J. W. Y.; Tang, B. Z., Aggregation-Induced Emission: New Vistas at the Aggregate Level. *Angew. Chem. Int. Ed.* **2020,** *59*, 9888–9907.

19. Peng, Q.; Shuai, Z., Molecular mechanism of aggregation-induced emission. *Aggregate* **2021,** *00*, e91.

20. Zhang, J.; Zhang, H.; Lam, J. W. Y.; Tang, B. Z., Restriction of Intramolecular Motion(RIM): Investigating AIE Mechanism from Experimental and Theoretical Studies. *Chem. Res. Chin. Univ.* **2021,** *37*, 1–15.

21. Peng, X.-L.; Ruiz-Barragan, S.; Li, Z.-S.; Li, Q.-S.; Blancafort, L., Restricted access to a conical intersection to explain aggregation induced emission in dimethyl tetraphenylsilole. *J. Mater. Chem. C* **2016,** *4*, 2802–2810.

22. Tu, Y.; Liu, J.; Zhang, H.; Peng, Q.; Lam, J. W. Y.; Tang, B. Z., Restriction of Access to the Dark State: A New Mechanistic Model for Heteroatom-Containing AIE Systems. *Angew. Chem. Int. Ed.* **2019,** *58*, 14911–14914.

23. Tu, Y.; Zhao, Z.; Lam, J. W. Y.; Tang, B. Z., Mechanistic connotations of restriction of intramolecular motions (RIM). *Natl. Sci. Rev.* **2021,** *8*, nwaa260.

24. Kang, M.; Zhang, Z.; Song, N.; Li, M.; Sun, P.; Chen, X.; Wang, D.; Tang, B. Z., Aggregation-enhanced theranostics: AIE sparkles in biomedical field. *Aggregate* **2020,** *1*, 80–106.

25. Shen, H.; Xu, C.; Sun, F.; Zhao, M.; Wu, Q.; Zhang, J.; Li, S.; Zhang, J.; Lam, J. W. Y.; Tang, B. Z., Metal‐Based Aggregation‐Induced Emission Theranostic Systems. *ChemMedChem* **2021,** *17*, e202100578.

26. Zuo, Y.; Shen, H.; Sun, F.; Li, P.; Sun, J.; Kwok, R. T. K.; Lam, J. W. Y.; Tang, B. Z., Aggregation-Induced Emission Luminogens for Cell Death Research. *ACS Bio & Med Chem Au* **2022,** 10.1021/acsbiomedchemau.1c00066.

27. Yang, Q.; Ma, H.; Liang, Y.; Dai, H., Rational Design of High Brightness NIR-II Organic Dyes with S-D-A-D-S Structure. *Acc. Mater. Res.* **2021,** *2*, 170–183.

28. Xu, W.; Wang, D.; Tang, B. Z., NIR-II AIEgens: A Win-Win Integration towards Bioapplications. *Angew. Chem. Int. Ed.* **2021,** *60*, 7476–7487.

29. Xu, P.; Kang, F.; Yang, W.; Zhang, M.; Dang, R.; Jiang, P.; Wang, J., Molecular engineering of a high quantum yield NIR-II molecular fluorophore with aggregation-induced emission (AIE) characteristics for in vivo imaging. *Nanoscale* **2020,** *12*, 5084–5090.

30. Liu, S.; Chen, C.; Li, Y.; Zhang, H.; Liu, J.; Wang, R.; Wong, S. T. H.; Lam, J. W. Y.; Ding, D.; Tang, B. Z., Constitutional Isomerization Enables Bright NIR‐II AIEgen for Brain‐Inflammation Imaging. *Adv. Funct. Mater.* **2019,** *30*, 1908125.

31. Xu, Y.; Zhang, H.; Zhang, N.; Xu, R.; Wang, Z.; Zhou, Y.; Shen, Q.; Dang, D.; Meng, L.; Tang, B. Z., An easily synthesized AIE luminogen for lipid droplet-specific super-resolution imaging and two-photon imaging. *Mater. Chem. Front.* **2021,** *5*, 1872–1883.

32. Zhao, Z.; Deng, C.; Chen, S.; Lam, J. W.; Qin, W.; Lu, P.; Wang, Z.; Kwok, H. S.; Ma, Y.; Qiu, H.; Tang, B. Z., Full emission color tuning in luminogens constructed from tetraphenylethene, benzo-2,1,3-thiadiazole and thiophene building blocks. *Chem. Commun. (Camb.)* **2011,** *47*, 8847–8849.

33. Li, K.; Qin, W.; Ding, D.; Tomczak, N.; Geng, J.; Liu, R.; Liu, J.; Zhang, X.; Liu, H.; Liu, B.; Tang, B. Z., Photostable fluorescent organic dots with aggregation-induced emission (AIE dots) for noninvasive long-term cell tracing. *Sci. Rep.* **2013,** *3*, 1150.

34. Li, Y.; Li, Z.; Ablekim, T.; Ren, T.; Dong, W. J., Rational design of tetraphenylethylene-based luminescent down-shifting molecules: photophysical studies and photovoltaic applications in a CdTe solar cell from small to large units. *Phys. Chem. Chem. Phys.* **2014,** *16*, 26193–26202.

35. Yang, Y.; Wang, S.; Lu, L.; Zhang, Q.; Yu, P.; Fan, Y.; Zhang, F., NIR-II Chemiluminescence Molecular Sensor for In Vivo High-Contrast Inflammation Imaging. *Angew. Chem. Int. Ed.* **2020,** *59*, 18380–18385.

36. Hatami, S.; Würth, C.; Kaiser, M.; Leubner, S.; Gabriel, S.; Bahrig, L.; Lesnyak, V.; Pauli, J.; Gaponik, N.; Eychmüller, A.; Resch-Genger, U., Absolute photoluminescence quantum yields of IR26 and IR-emissive Cd1−xHgxTe and PbS quantum dots – method- and material-inherent challenges. *Nanoscale* **2015,** *7*, 133–143.

37. Zheng, X.; Peng, Q.; Zhu, L.; Xie, Y.; Huang, X.; Shuai, Z., Unraveling the aggregation effect on amorphous phase AIE luminogens: a computational study. *Nanoscale* **2016,** *8*, 15173–15180.

38. Maes, B.; Ciscato, L. F. M. L.; Augusto, F. A.; Weiss, D.; Bartoloni, F. H.; Albrecht, S.; Brandl, H.; Zimmermann, T.; Baader, W. J., The chemiluminescent peroxyoxalate system: state of the art almost 50 years from its discovery. *ARKIVOC* **2012,** *3*, 391–430.

39. Wang, Z.; Huang, J.; Huang, J.; Yu, B.; Pu, K.; Xu, F.-J., Chemiluminescence: From mechanism to applications in biological imaging and therapy. *Aggregate* **2021,** *2*, e140.

40. Shuhendler, A. J.; Pu, K.; Cui, L.; Uetrecht, J. P.; Rao, J., Real-time imaging of oxidative and nitrosative stress in the liver of live animals for drug-toxicity testing. *Nat. Biotechnol.* **2014,** *32*, 373–380.

41. Zhen, X.; Zhang, C.; Xie, C.; Miao, Q.; Lim, K. L.; Pu, K., Intraparticle Energy Level Alignment of Semiconducting Polymer Nanoparticles to Amplify Chemiluminescence for Ultrasensitive In Vivo Imaging of Reactive Oxygen Species. *ACS Nano* **2016,** *10*, 6400–6409.

42. Mao, D.; Wu, W.; Ji, S.; Chen, C.; Hu, F.; Kong, D.; Ding, D.; Liu, B., Chemiluminescence-Guided Cancer Therapy Using a Chemiexcited Photosensitizer. *Chem* **2017,** *3*, 991–1007.